
S4Fusion: Saliency-aware Selective State Space Model for Infrared Visible Image Fusion

Haolong Ma¹, Hui Li¹, Chunyang Cheng¹, Gaoang Wang², Xiaoning Song¹, Xiaojun Wu¹

¹Jiangnan University, ²Zhejiang University
{lihui.cv, wu_xiaojun, x.song}@jiangnan.edu.cn
ninesxd@qq.com, chunyang_cheng@163.com, gaoangwang@intl.zju.edu.cn

Abstract

As one of the tasks in Image Fusion, Infrared and Visible Image Fusion aims to integrate complementary information captured by sensors of different modalities into a single image. The Selective State Space Model (SSSM), known for its ability to capture long-range dependencies, has demonstrated its potential in the field of computer vision. However, in image fusion, current methods underestimate the potential of SSSM in capturing the global spatial information of both modalities. This limitation prevents the simultaneous consideration of the global spatial information from both modalities during interaction, leading to a lack of comprehensive perception of salient targets. Consequently, the fusion results tend to bias towards one modality instead of adaptively preserving salient targets. To address this issue, we propose the Saliency-aware Selective State Space Fusion Model (S4Fusion). In our S4Fusion, the designed Cross-Modal Spatial Awareness Module (CMSA) can simultaneously focus on global spatial information from both modalities while facilitating their interaction, thereby comprehensively capturing complementary information. Additionally, S4Fusion leverages a pre-trained network to perceive uncertainty in the fused images. By minimizing this uncertainty, S4Fusion adaptively highlights salient targets from both images. Extensive experiments demonstrate that our approach produces high-quality images and enhances performance in downstream tasks.

1 Introduction

As an image processing technique, Infrared and Visible Image Fusion aims to integrate information from different modalities captured by various sensors in the same scene, generating a comprehensive and informative image [18; 51; 52]. This technique has been widely used in various scenarios such as image restoration[5], UAV reconnaissance[16; 32], image registration[15], and can be combined with downstream tasks like image segmentation[35], detection[47; 38], and object tracking[25]. Visible images possess rich texture details and high resolution but are susceptible to illumination and occlusion, leading to loss of salient information[46]. Infrared images, on the other hand, rely on thermal radiation information to capture salient details under extreme conditions (e.g., low light) but are prone to noise[43]. Thus, integrating complementary information from both modalities comprehensively is essential for better reconstructing real-world scenes.

Originating from control systems, Selective State Space Models (SSSM) are a type of State Space Model (SSM)[8; 9]. For IVIF tasks, selectively highlighting information from both source images is crucial[18]. Previous works overlook the importance of considering global spatial information during the interaction between the two modalities[36; 17; 26]. For example, while Cross Attention[45] effectively captures inter-modal information, it can only focus on the spatial information of the

opposite modality during interactions. This means that it neglects the spatial information within its own modality during the interaction, which leads to a failure in comprehensively perceiving complementary information based on its own global space. This limitation is particularly critical for tasks like infrared and visible image fusion (IVIF), where the two modalities have highly complementary information.

Therefore, it is essential to design a module that can simultaneously focus on the spatial information of the images while perceiving and selecting the most beneficial complementary information between the two modalities. To address this, we designed a new module called Cross-Modal Spatial Awareness Module (CMSA). This module can simultaneously facilitate interactions between modalities and within the spatial domains of each modality, thereby enhancing the perception of salient targets.

To drive the CMSA to adaptively highlight salient information, we use a pre-trained ResNet50 network as a supervisory signal. In real-world scenes, the information should be deterministic and structured rather than random noise. Building on this observation, we designed a novel loss function called perception-enhanced loss at the decision layer of the pre-trained network. This function adaptively highlights salient targets and removes redundant information by minimizing the uncertainty perception of the pre-trained neural network on the fused image. Finally, we applied the designed CMSA module to a multi-scale network structure and proposed the Saliency-aware Selective State Space Model (S4Fusion) for IVIF task. The contributions of this paper can be summarized as follows:

(I) We designed a module called Cross-Modal Spatial Awareness Module (CMSA). This module captures information from both modalities spaces and their interrelations simultaneously, with linear complexity. It selectively preserves salient information while eliminating redundant details.

(II) To drive the CMSA to adaptively highlight salient information, we developed a novel loss function at the decision layer to simulate human visual perception. This function aims to highlight salient information adaptively, resulting in images that better align with human visual perception.

(III) We conducted extensive experiments to validate the effectiveness of our method, including qualitative evaluations, quantitative evaluations, and evaluations involving integration with downstream tasks.

2 Related Work

2.1 Infrared and Visible Image Fusion

With the rise of deep learning, an increasing number of researchers are adopting deep learning methods to study IVIF[12; 13; 14]. These methods can generally be classified into three categories: generative models[22; 23], autoencoder-based models[12; 13], and end-to-end models[44; 48]. Generative models often suffer from unstable training, autoencoder-based methods offer more stable training but still rely to some extent on handcrafted fusion strategies[43]. End-to-end methods, on the other hand, often design loss functions at the shallow pixel level, which can still be considered as handcrafted fusion rules, limiting the network’s adaptability.

To enable models to adaptively integrate information from two source images, many end-to-end models make attempts[18; 17; 33]. Among them, U2Fusion[41] achieves excellent results by using features from a pre-trained VGG16 network as a supervisory signal. However, due to the lack of consideration for highlighting salient targets adaptively, it weakened the preservation of saliency information. Therefore, we design a new perception-enhanced loss, simulating human visual perception at the decision layer of the pre-trained model, to highlight salient targets.

2.2 Selective State Space Model

Recently, State Space Models attract increasing interest from researchers across various fields, demonstrating significant potential in NLP and CV[21; 30; 24]. Early works like LSSL[9], when combined with HiPPO initialization[7], exhibited powerful capabilities in capturing long-range dependencies. With the emergence of Mamba[37; 6], the Selective State Space Model was introduced and achieved remarkable success in NLP. The introduction of VMamba[20] brought Mamba into the field of computer vision (CV). Its powerful global receptive field, rapid inference speed, and lack of need for positional embedding have inspired many related works in CV.

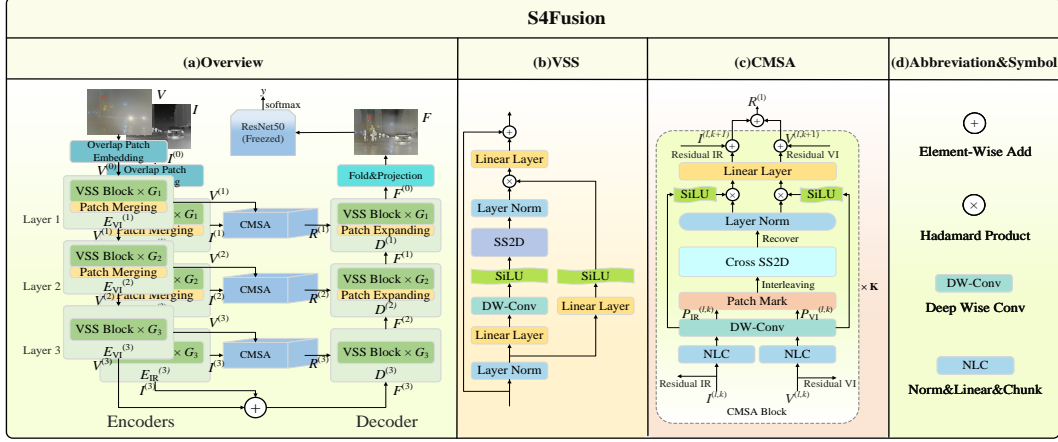


Figure 1: The architecture of S4Fusion with the number of layers $N = 3$. (a) depicts the overall architecture of S4Fusion. G_i represents the number of i -th layer VSS Blocks. (b) shows the internal workflow of the VSS Block. (c) illustrates the structure of the CMSA in the l -th layer, consisting of K Cross-Modal Spatial Awareness Module Blocks. (d) provides notations and abbreviations.

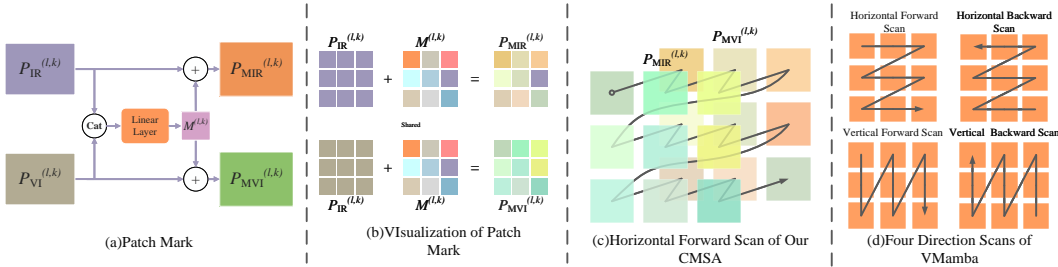


Figure 2: Figures of Patch Mark and Cross SS2D. (a) and (b) demonstrate the computation process of Patch Mark. Panel (c) illustrates the Cross SS2D scanning trajectory in the Horizontal Forward direction. (d) shows the four scanning trajectories of SS2D as described in the original VMamba paper.

In Image Fusion, some works start to combine with Mamba[26; 2]. For example, FusionMamba[26] designed FSSM, inspired by cross-attention, which achieved notable success in the hyperspectral pansharpening task. However, these methods focus primarily on inter-modal interactions, overlooking the importance of simultaneously considering information from both modality spaces. To address this, we propose a new module called Cross-Modal Spatial Awareness Module (CMSA). CMSA can perform inter-modal interactions and interactions within each modality space in a single stage, enabling comprehensive perception of salient information in both spatial and modal dimensions.

3 Proposed Method

In this section, we delve into the detailed process of our approach. As shown in Fig.1, following the form of UNet[1; 30], our model adopts a multi-scale structure to capture image information at different scales. Our model primarily consists of two types of modules: VSS Block[20] and CMSA. Overlap Patch Embedding and Fold & Output Projection are utilized at the input and output ends of the model to encode overlapping patches and integrate outputs across spatial and channel dimensions. Infrared and visible images are processed in two separate streams, each with its own independent encoder to extract features specific to their respective modalities. For simplicity, we assume the encoder and decoder each have N layers.

3.1 Preliminary

3.1.1 SSM

The State Space Model (SSM) initially served as a time-series processing model, mapping input sequences $x(t)$ to output sequences $y(t)$ through hidden states $h(t)$ to memorize and capture temporal relationships. Formally, SSM can be expressed by the following two equations: $h'(t) = Ah(t) + Bx(t)$; $y(t) = Ch(t)$, where A , B , and C are parameters. A controls the update of hidden states, while B and C govern how data flows into and out of hidden states. Subsequently, to better handle discrete data in real-world scenarios (such as text), the time step parameter Δ is introduced to control the time interval. Through zero-order hold, SSM is further discretized into the following form[8]: $h_t = \bar{A}h_{t-1} + \bar{B}x_t$; $y_t = Ch_t$, where \bar{A} and \bar{B} are counterparts of A and B after zero-order hold, with $\bar{A} = \exp(\Delta A)$ and $\bar{B} = \Delta B$.

3.1.2 Mamba and VMamba

Mamba transforms the original parameters A , B , and C into context-dependent parameters, making SSM selective to inputs[37]. Specifically, at time t , the computation process of SSM from input to output utilizes parameters A , B , and C derived from the input x_t .

Subsequently, VMamba[30] introduced Mamba into the realm of CV for the first time and designed the SS2D module to address the inability of Mamba to handle image data. As shown in Fig.2(d), VMamba non-overlappingly divides the image into patches and flattens them into sequences in four different directions. These sequences are then individually inputted into Mamba Blocks for computation and finally aggregated to extract features.

3.2 Encoder and Decoder

We use VSS Blocks[30] for feature extraction and image reconstruction for each modality. As shown in Fig.1(b), the VSS Block adopts a design similar to Mamba Block, resembling the structure of ResNet. Within it, SS2D has a global receptive field. We employ VSS Blocks as encoders for each modality to extract shallow features within their respective modalities. These features will be further utilized for deeper interactions. Multiple VSS Blocks serve as encoders at each scale. Let I and V denote the two original images. After applying Overlap Patch Embedding, we obtain $I^{(0)}, V^{(0)} \in \mathbb{R}^{H \times W \times C}$, which represent the infrared and visible features, respectively.

$$I^{(l)} = \text{Down}^{(l)}(E_{\text{IR}}^{(l)}(I^{(l-1)})), V^{(l)} = \text{Down}^{(l)}(E_{\text{VI}}^{(l)}(V^{(l-1)})), \text{ where } l \in \{1, 2, \dots, N\} \quad (1)$$

where $E_{\text{IR}}^{(l)}(\cdot)$ and $E_{\text{VI}}^{(l)}(\cdot)$ represent the encoder for the infrared and visible modalities at the l -th layer. $\text{Down}^{(l)}(\cdot)$ denotes Patch Merging or *Identity* operation. As depicted in Fig.1(a), $\text{Down}^{(l)}(\cdot) = \text{Identity}(\cdot)$ only when $l = N$.

For the decoder at the l -th layer, it takes the fused feature $R^{(l)}$ and the output from the previous scale $F^{(l)}$ as input to reconstruct the image feature at that scale.

$$F^{(l-1)} = D^{(l)}(UP^{(l)}(F^{(l)}) + R^{(l)}), \text{ where } F^{(N)} = I^{(N)} + V^{(N)}, l \in \{1, 2, \dots, N\} \quad (2)$$

where $UP^{(l)}$ represents Patch Expanding or *Identity* operation. Similar to Down , $UP^{(l)}(\cdot) = \text{Identity}(\cdot)$ only at the N -th layer.

Finally, the output $F^{(0)}$ undergoes folding to remove overlaps and is linearly mapped to integrate channels, resulting in the final fused image F .

3.3 Cross-Modal Spatial Awareness Module

The Cross-Modal Spatial Awareness Module (CMSA) is employed to interact with features from the infrared and visible modalities at various scales, thereby efficiently perceiving salient information. Specifically, CMSA consists of K CMSA Blocks (CMSAB).

For ease of discussion, in this section, we will use the k -th CMSAB in the l -th layer as an example. And, we also denote $V^{(l,0)} = V^{(l)}$ and $I^{(l,0)} = I^{(l)}$, $k \in \{1, 2, \dots, K\}$, $l \in \{1, 2, \dots, N\}$.

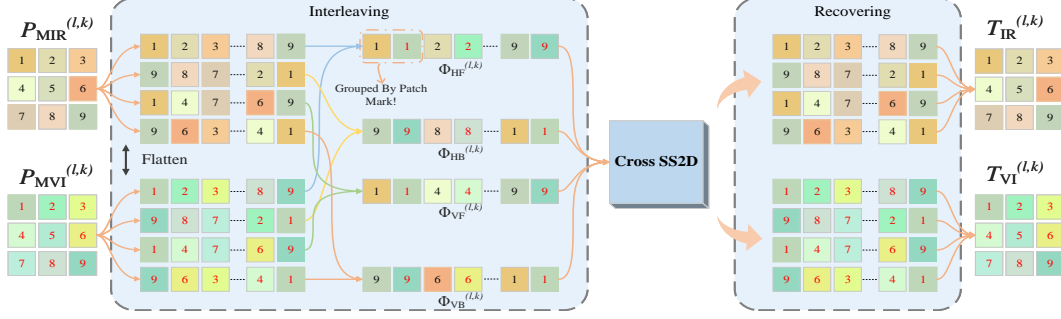


Figure 3: Demonstration of the Interleaving and Recovering processes. The numbers in different colors represent patches from different modalities, and identical numbers denote patches from the same position in the feature maps.

As depicted in Fig.1(c), features from the two modalities (i.e. $I^{(l,k)}, V^{(l,k)}$) are first split into two branches separately using Layer Norm and a linear mapping. One branch is used for gating mechanism, while the other passes through a shared 3×3 depth-wise convolution to extract features, denoted as $P_{IR}^{(l,k)}$ and $P_{VI}^{(l,k)}$ respectively. These features are then utilized for subsequent deep-level feature interaction. This process consists of four steps: Patch Mark, Interleaving, Cross SS2D, and Recovering. Subsequently, the two obtained outputs go through a layer norm, a linear layer and a residual connection, yielding the outputs $I^{(l,k+1)}$ and $V^{(l,k+1)}$ of the k -th CMSAB. At the end of the K -th CMSAB, the two deeply interacted features are element-wise summed: $R^{(l)} = I^{(l,K)} + V^{(l,K)}$, resulting in the output $R^{(l)}$ of the l -th CMSA.

3.3.1 Patch Mark

Patch Mark, similar to positional encoding, is used to group patches from the same positions in the two modalities. Specifically, as shown in Fig.2(a, b), Patch Mark concatenates the two inputs along the channel dimension and then applies a linear layer to generate a mark for each patch position. Consequently, patches from the same position in each modality are labeled with the same mark, resulting in $P_{MIF}^{(l,k)}$ and $P_{MVF}^{(l,k)}$:

$$M^{(l,k)} = \text{linear}^{(l,k)}([P_{IR}^{(l,k)}; P_{VI}^{(l,k)}]) \quad (3)$$

$$P_{MIR}^{(l,k)} = P_{IR}^{(l,k)} + M^{(l,k)}, P_{MVI}^{(l,k)} = P_{VI}^{(l,k)} + M^{(l,k)} \quad (4)$$

where $[\cdot; \cdot]$ denotes concatenation along the channel dimension, and $M^{(l,k)}$ represents the mark at l -th layer and k -th CMSAB. Patch Mark effectively groups patches from the same positions in both modalities, enabling a clear distinction between inter-modal interactions and spatial interactions.

3.3.2 Interleaving

The Interleaving operation flattens the features of two modalities into sequences in four directions. Subsequently, sequences from the same unfolding direction in the two modalities are merged alternately into a new sequence. As depicted in Fig.3, the features are initially unfolded into eight sequences based on combinations of vertical, horizontal, forward, and backward directions. Then, sequences with the same flattening direction are interleaved to form four long sequences: $\Phi_{HF}^{(l,k)}, \Phi_{HB}^{(l,k)}, \Phi_{VF}^{(l,k)}, \Phi_{VB}^{(l,k)} = \text{inter}(P_{MIR}^{(l,k)}, P_{MVI}^{(l,k)})$ where inter denotes the interleaving operation. Subscripts HF and VB represent Horizontal Forward and Vertical Backward flattening directions, respectively, and similarly for others. Taking $\Phi_{HF}^{(l,k)}$ in Fig.3 as an example, due to Patch Mark grouping patches, patches with the same number can be considered as a whole. Each grouped patches is considered as a single entity, representing the spatial dimension from left to right across the entire sequence.

3.3.3 Cross SS2D

Cross SS2D is employed to capture contextual relationships on interleaved long sequences. Cross SS2D first computes Δ , B , and C using different parameters for each modality. Subsequently, these computed parameters are interleaved so that each patch on every sequence corresponds to its own modality-specific parameters. While this approach may seem to hinder interactions between modalities, both modalities share a common hidden state. Using modality-specific parameters allows selective compression of relevant information within each modality based on information from the other modality, or selective extraction of relevant information from the hidden state. As illustrated in Fig.2(c), from the modality perspective, Cross SS2D iteratively traverses between the two modalities to accomplish inter-modality interactions. Moreover, thanks to Patch Mark, Cross SS2D can consider grouped patches as a single entity, enabling the consideration of saliency information from a global spatial perspective. This enables comprehensive perception and integration of saliency information within both modalities: $F_{\text{HF}}^{(l,k)}, F_{\text{HB}}^{(l,k)}, F_{\text{VF}}^{(l,k)}, F_{\text{VB}}^{(l,k)} = \text{CSS2D}(\Phi_{\text{HF}}^{(l,k)}, \Phi_{\text{HB}}^{(l,k)}, \Phi_{\text{VF}}^{(l,k)}, \Phi_{\text{VB}}^{(l,k)})$, where CSS2D denotes Cross SS2D.

Algorithm 1 describes the Cross SS2D algorithm in a manner similar to Mamba[6]. Assuming the input sequence length is $2L$, where L is the number of patches in the feature map, H and B represent the size of the hidden state in SSM and the batch size, respectively. $S(\cdot)$ denotes a linear layer, where the first letter in the subscript indicates the perceived parameter (e.g. B and C), and the second letter denotes the modality (i.e. I and V). τ_{Δ} represents softplus function. $\text{Inter}(\cdot, \cdot)$ represents the interleaving arrangement of linear layers from different modalities, corresponding to the input sequence interleaved with modalities. This means that parameters Δ , B , C , and A have different perceptions for different modalities. $\text{discretize}(\cdot, \cdot, \cdot)$ represents the process of discretization, calculated according to section 3.1.1. We provide a more detailed explanation of these parameters in the appendix A.3.

Algorithm 1 Cross SS2D

Input: \mathbf{x} : ($B, 2L, C$)
Output: \mathbf{y} : ($B, 2L, C$)
 $\mathbf{A} : (B, L, H) \leftarrow \text{Parameter}$
 $\mathbf{B} : (B, 2L, H) \leftarrow \text{Inter}(S_{\text{BI}}, S_{\text{BV}})(\mathbf{x})$
 $\mathbf{C} : (B, 2L, H) \leftarrow \text{Inter}(S_{\text{CI}}, S_{\text{CV}})(\mathbf{x})$
 $\underline{\Delta} : (B, 2L, H) \leftarrow \tau_{\Delta}(\text{Parameter} + \text{Inter}(S_{\Delta\text{I}}, S_{\Delta\text{V}})(\mathbf{x}))$
 $\mathbf{A}, \mathbf{B} : (B, 2L, C, H) \leftarrow \text{discretize}(\underline{\Delta}, \mathbf{A}, \mathbf{B})$
 $\mathbf{y} \leftarrow \text{SSM}(\mathbf{A}, \mathbf{B}, \mathbf{C})(\mathbf{x})$
return \mathbf{y}

3.3.4 Recovering

Recovering is responsible for disassembling the features after Cross SS2D interaction and restoring them to their original feature map shapes. This process is illustrated in Fig.2. Initially, the features are disassembled into sequences organized in their original four directions. Subsequently, patches at corresponding positions within each modality are added together and combined to reconstruct the original shape of the feature map: $T_{\text{IR}}^{(l,k)}, T_{\text{VI}}^{(l,k)} = \text{Recover}(F_{\text{HF}}^{(l,k)}, F_{\text{HB}}^{(l,k)}, F_{\text{VF}}^{(l,k)}, F_{\text{VB}}^{(l,k)})$. The recovered features, as shown in Fig.1(c), are passed through layer normalization, a gating mechanism, and residual connections to obtain the output $V^{(l,k+1)}, I^{(l,k+1)}$ of the k -th CMSAB layer.

3.4 Loss

The loss function comprises four components: a L1 loss \mathcal{L}_{L1} , a structural similarity loss $\mathcal{L}_{\text{ssim}}$, a gradient loss $\mathcal{L}_{\text{grad}}$, and our proposed perceptual enhancement loss \mathcal{L}_{per} . The $\mathcal{L}_{\text{total}}$ is

$$\mathcal{L}_{\text{total}} = \mathcal{L}_{\text{per}} + \alpha_1 \mathcal{L}_{\text{L1}} + \alpha_2 \mathcal{L}_{\text{ssim}} + \alpha_3 \mathcal{L}_{\text{grad}} \quad (5)$$

where α_1 , α_2 , and α_3 are hyperparameters used to balance each loss.

$\mathcal{L}_{\text{ssim}}$ and \mathcal{L}_{L1} are inspired by U2Fusion[41]. We use a pretrained ResNet50 to measure the amount of information of the two original images, obtaining estimates ω_1 and ω_2 to compute \mathcal{L}_{L1} and $\mathcal{L}_{\text{ssim}}$.

Table 1: Quantitative Comparison on MSRS[34] and RoadScene[42] datasets

		MSRS[34]						RoadScene[42]					
Method	year	MI	SF	AG	SSIM	VIF	Qabf	MI	SF	AG	SSIM	VIF	Qabf
DeFusion	2022	3.35	8.61	2.78	0.46	0.76	0.53	2.96	8.82	3.55	0.43	0.51	0.37
U2Fusion	2022	2.28	6.21	1.98	0.32	0.52	0.29	2.68	12.41	5.05	0.50	0.54	0.49
ReCoNet	2022	2.28	9.98	3.00	0.20	0.49	0.40	3.13	9.01	3.78	0.45	0.54	0.38
SemLA	2023	2.45	6.34	2.24	0.37	0.61	0.29	2.75	13.86	4.26	0.39	0.49	0.30
DDFM	2023	2.73	7.39	2.52	0.45	0.74	0.47	1.85	11.41	4.66	0.04	0.10	0.15
IRFS	2023	2.15	9.89	3.16	0.43	0.74	0.48	2.82	10.21	3.93	0.49	0.57	0.42
DATFuse	2023	<u>3.89</u>	10.93	3.57	0.45	0.91	<u>0.64</u>	<u>3.70</u>	11.34	4.07	<u>0.46</u>	0.59	0.47
EMMA	2024	4.24	<u>11.56</u>	<u>3.79</u>	<u>0.48</u>	<u>0.97</u>	0.64	3.27	<u>15.82</u>	<u>6.14</u>	0.46	<u>0.62</u>	0.44
S4Fusion	-	3.81	11.68	3.80	0.49	1.00	0.68	3.75	16.16	6.24	0.50	0.79	0.61

To simulate human visual perception and highlight saliency, we design \mathcal{L}_{per} loss at the decision layer of the pretrained ResNet50[10]. For the fusion result F , if its salient targets are more prominent, it should contain more definitive information rather than noise. We assume y as the probability distribution of ResNet50’s estimates for F over 1000 categories. The Entropy of this distribution estimates the certainty, reflecting the saliency target perception: $\mathcal{L}_{\text{per}} = -\sum_{i=1}^{1000} y_i \log(y_i)$, where $y = \text{softmax}(\text{ResNet50}(F))$. \mathcal{L}_{per} minimizes this uncertainty to highlight salient objects in the two original images. However, focusing solely on salient targets may lead to loss of texture details and degrade image quality. Moreover, excessive convergence of \mathcal{L}_{per} can result in image quality deterioration. Therefore, we introduce $\mathcal{L}_{\text{grad}}$ to preserve texture details while restraining the perceptual enhancement loss: $\mathcal{L}_{\text{grad}} = |||\nabla F| - \max(|\nabla I|, |\nabla V|)|_1$. Where ∇ represents the Sobel operator used to compute the edge texture information of the image.

Table 2: Quantitative Comparison on M3FD[19] Dataset

Dataset	MI	SF	AG	SSIM	VIF	Qabf
DeFusion	2.89	7.75	2.79	0.42	0.53	0.34
U2Fusion	2.62	11.21	4.26	0.49	0.61	0.53
ReCoNet	2.99	11.06	4.23	0.43	0.57	0.49
SemLA	2.61	7.37	2.75	0.28	0.38	0.18
DDFM	2.68	9.58	3.38	0.31	0.49	0.38
IRFS	2.76	10.92	3.68	0.48	0.62	0.50
DATFuse	<u>4.09</u>	10.97	3.70	0.46	0.63	0.50
EMMA	3.81	15.88	5.72	0.46	<u>0.75</u>	0.59
S4Fusion	4.43	<u>15.36</u>	<u>5.31</u>	<u>0.48</u>	0.91	0.66

Table 3: Various ablation experiments conducted on MSRS[34]. "Number" represents the experiment ID, and "→" indicates module replacement.

Number	Method	MI	AG	VIF	Qabf	SSIM	SF
Exp.1	CMSA→ADD	3.24	3.78	0.84	0.61	0.46	11.52
Exp.2	CMSA→CNN	3.61	3.70	0.91	0.63	0.47	<u>11.66</u>
Exp.3	CMSA→CA	2.83	3.53	0.66	0.47	0.39	11.62
Exp.4	CMSA→FSSM	3.5	3.77	<u>0.98</u>	0.64	<u>0.48</u>	11.50
Exp.5	w/o PM	3.27	<u>3.78</u>	0.85	0.63	0.46	11.49
Exp.6	w/o Per	<u>3.71</u>	3.75	0.97	<u>0.65</u>	0.48	11.03
Exp.7	S4Fusion	3.81	3.80	1.00	0.68	0.49	11.68

Table 4: AP@50 values for MM Detection on M3FD[19] Dataset

	Car	People	Truck	Lamp	Motor	Bus	mAP@50
IR	86.1	77.0	74.9	51.5	62.1	91.0	73.8
VI	89.4	66.8	<u>79.3</u>	<u>80.4</u>	68.6	91.5	79.3
DeFusion	89.6	75.0	80.4	77.8	68.2	91.9	80.5
DDFM	90.0	73.8	77.5	77.6	71.7	<u>92.0</u>	80.4
ReCoNet	89.9	72.8	78.3	78.6	69.9	90.8	80.1
SemLA	87.4	71.4	75	73.2	65.9	90.2	77.2
U2Fusion	90.1	<u>75.1</u>	78.4	77.8	65.4	90.6	79.6
IRFS	90.4	73.9	79	78.6	73.3	90.9	<u>81.0</u>
DATFuse	88.8	74.4	79.6	73.1	69.8	91.6	79.6
EMMA	89.2	72.2	78.2	71.9	67.1	90.5	78.2
S4Fusion	<u>90.1</u>	72.8	78.4	80.7	<u>72.4</u>	93.4	81.3

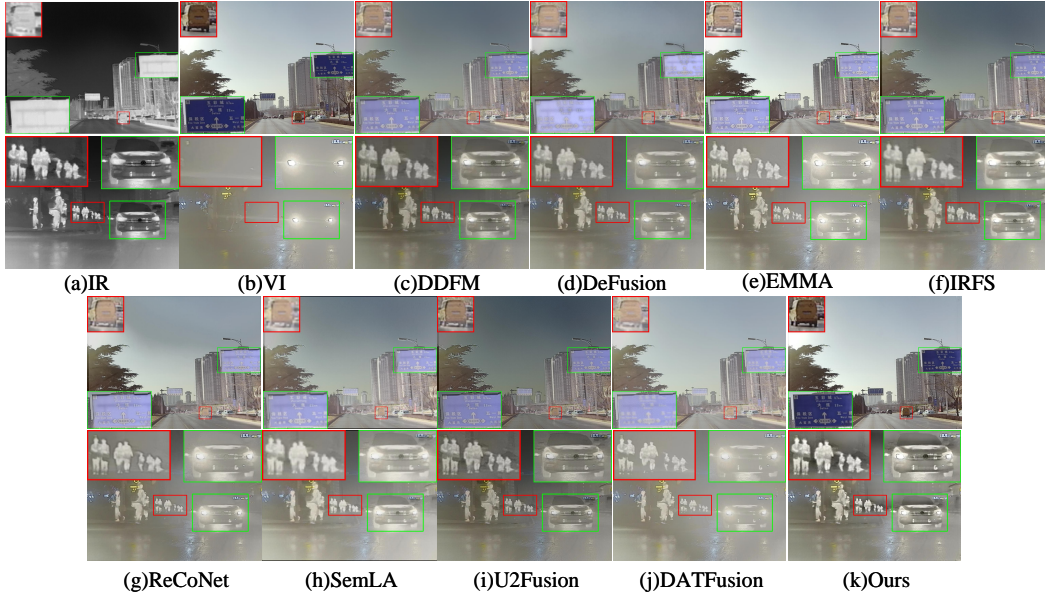


Figure 4: Qualitative comparison of the original images and the results of all methods on "03989" and "00338" from M3FD[19].

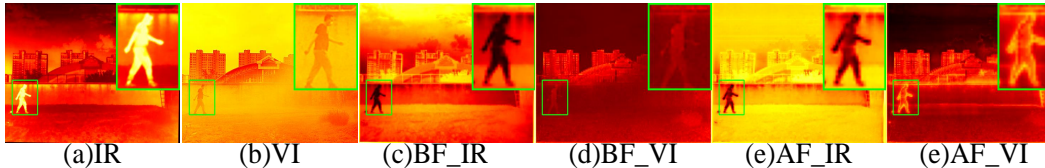


Figure 5: Visualization of the feature maps before and after the second-layer CMSA in M3FD[19] for "00388", along with the original images. AF and BF represent "After" and "Before", indicating the feature maps post- and pre-CMSA, respectively.

4 Experiment

Existing datasets suffer from distributional biases, yet the objectives of significance are diverse. To address this, we amalgamate the training sets of MSRS[34], 70% of M3FD[19], and 70% of RoadScene[42] to form a sufficiently diversified dataset for training, with the remaining portions reserved for testing and validation. We set the hyperparameters α_1 , α_2 , and α_3 to 15, the number of layers N to 3, the number of CMSAB K to 3, and the number of VSS Blocks in both Encoders and Decoder to $G = [1, 2, 1]$. For further training details, please refer to the appendixA.1. We compare our approach with eight state-of-the-art methods, namely U2Fusion[41], DeFusion[17], DDFM[50], DATFusion[36], SemLA[40], ReCoNet[11], IRFS[3], and EMMA[49]. For quantitative evaluation, we employ six metrics according to previous works[12; 18; 49]: Mutual Information (MI)[28], Spatial Frequency (SF)[4], Structural Similarity Index Measure[39] (SSIM), Visual Information Fidelity [31](VIF), Average Gradient (AG), and Qabf[27]. For downstream tasks, we utilize AP@50 on M3FD for Multi-Modality Object detection task evaluation. For specific details, please refer to the appendixA.1.

5 Qualitative Comparison

As illustrated in Fig.4, our approach remains effective in highlighting salient objects clearly while preserving as much texture detail as possible. Other methods, such as ReCoNet and DeFusion, fail to achieve comparable clarity. Conversely, when faced with excessive noise in infrared images, our

method avoids excessive bias towards the infrared modality. In contrast, methods like DeFusion, IRFS, and U2Fusion suffer from a lack of adaptability, leading to blurred text on road signs due to over-reliance on the infrared modality. More qualitative results are provided in the appendixA.2.

6 Quantitative Comparison

As shown in Table.1 and 2, we conducted quantitative testing on three datasets. Compared to other methods, ours yielded outstanding results. Our method demonstrated higher SSIM, AG, and SF, indicating that it preserves more texture details and structure information and aligns better with human perception. Additionally, our method also achieved good results in Qabf, VIF, and MI, indicating that it retains more original image information.

As shown in Table. 4, our approach achieves excellent results in multimodal object detection. Our mAP@50 surpasses other methods, indicating that overall, our approach effectively highlights salient objects. While our method also shows some effectiveness in the People and Truck categories, slight deviations due to inherent biases in ResNet50 lead to slightly inferior performance compared to other methods.

7 Ablation Study

To demonstrate the validity of our approach, we conducted ablation experiments as shown in Table 3. In Exp.6, we removed the proposed perceptual enhancement loss function while maintaining the remaining experimental configurations to verify its effectiveness. The results confirmed the efficacy of our proposed perceptual enhancement loss. Regarding module design, in Exp.1-4, we replaced the proposed CDM with ADD, Cross Attention[45], CNN[10], and FSSM[26], respectively, while adjusting parameters to maintain consistency of model size with our proposed method. Among these, ADD, which directly adds features, yielded inferior results due to the lack of interaction between features. Cross Attention(CA) performed poorly due to its lack of spatial interaction and certain incompatibilities with SSM. CNN suffered from information loss to some extent due to the lack of a global receptive field, while FSSM lost significant saliency information as it couldn't simultaneously interact within and between modalities. In Exp.5, we removed Patch Mark to assess its role in distinguishing spatial and inter-modality interactions in Cross SS2D. The results indicated a significant decrease in information retention and fidelity when Patch Mark was absent.

8 Visualization

To investigate how CMSA operates, we analyzed the features pre- and post-processing. Fig.5 illustrates the changes observed. Prior to CMSA processing, visible features displayed a blurry human figure and unclear background, whereas infrared features showed the opposite characteristics. Following CMSA processing, infrared features highlighted the human figure against the background, while both human figures and backgrounds in the visible spectrum were improved. This showcases the CMSA module's capacity to capture and integrate information from different modalities, facilitating the enhancement of significant elements through their synergistic interaction.

9 Conclusion

This paper tackles the challenge of adapting reinforcement saliency objectives within pre-trained neural networks' decision layers for perceiving the uncertainty of fused images. Furthermore, to enhance the integration of complementary information across modalities at a global level, we introduce a one-stage fusion module, named CMSA. This module addresses the lack of global space information in previous methods during the intermodal interaction. Finally, we conduct extensive experiments to validate the effectiveness of our proposed approach.

References

- [1] H. Cao, Y. Wang, J. Chen, D. Jiang, X. Zhang, Q. Tian, and M. Wang. Swin-unet: Unet-like pure transformer for medical image segmentation. In *European conference on computer vision*, pages 205–218. Springer, 2022.
- [2] Z. Cao, X. Wu, L.-J. Deng, and Y. Zhong. A novel state space model with local enhancement and state sharing for image fusion. *arXiv preprint arXiv:2404.09293*, 2024.
- [3] W. Di, L. Jinyuan, R. Liu, and F. Xin. An interactively reinforced paradigm for joint infrared-visible image fusion and saliency object detection. In *Information Fusion*, 2023.
- [4] A. M. Eskicioglu and P. S. Fisher. Image quality measures and their performance. *IEEE Transactions on communications*, 43(12):2959–2965, 1995.
- [5] K. Falahkheirkhah, K. Yeh, M. P. Confer, and R. Bhargava. Drb-net: Dilated residual block network for infrared image restoration. In *International Symposium on Visual Computing*, pages 104–115. Springer, 2022.
- [6] A. Gu and T. Dao. Mamba: Linear-time sequence modeling with selective state spaces. *arXiv preprint arXiv:2312.00752*, 2023.
- [7] A. Gu, T. Dao, S. Ermon, A. Rudra, and C. Ré. Hippo: Recurrent memory with optimal polynomial projections. *Advances in neural information processing systems*, 33:1474–1487, 2020.
- [8] A. Gu, K. Goel, and C. Ré. Efficiently modeling long sequences with structured state spaces. *arXiv preprint arXiv:2111.00396*, 2021.
- [9] A. Gu, I. Johnson, K. Goel, K. Saab, T. Dao, A. Rudra, and C. Ré. Combining recurrent, convolutional, and continuous-time models with linear state space layers. *Advances in neural information processing systems*, 34:572–585, 2021.
- [10] K. He, X. Zhang, S. Ren, and J. Sun. Deep residual learning for image recognition. In *Proceedings of the IEEE conference on computer vision and pattern recognition*, pages 770–778, 2016.
- [11] Z. Huang, J. Liu, X. Fan, R. Liu, W. Zhong, and Z. Luo. Reconet: Recurrent correction network for fast and efficient multi-modality image fusion. In *European conference on computer Vision*, pages 539–555. Springer, 2022.
- [12] H. Li and X.-J. Wu. Densefuse: A fusion approach to infrared and visible images. *IEEE Transactions on Image Processing*, 28(5):2614–2623, 2018.
- [13] H. Li, X.-J. Wu, and T. Durrani. Nestfuse: An infrared and visible image fusion architecture based on nest connection and spatial/channel attention models. *IEEE Transactions on Instrumentation and Measurement*, 69(12):9645–9656, 2020.
- [14] H. Li, X.-J. Wu, and J. Kittler. Rfn-nest: An end-to-end residual fusion network for infrared and visible images. *Information Fusion*, 73:72–86, 2021.
- [15] H. Li, J. Zhao, J. Li, Z. Yu, and G. Lu. Feature dynamic alignment and refinement for infrared-visible image fusion: Translation robust fusion. *Information Fusion*, 95:26–41, 2023.
- [16] J. Li, Y. Peng, and T. Jiang. Embedded real-time infrared and visible image fusion for uav surveillance. *Journal of Real-Time Image Processing*, 18(6):2331–2345, 2021.
- [17] P. Liang, J. Jiang, X. Liu, and J. Ma. Fusion from decomposition: A self-supervised decomposition approach for image fusion. In *European Conference on Computer Vision*, pages 719–735. Springer, 2022.
- [18] J. Liu, R. Dian, S. Li, and H. Liu. Sgfusion: A saliency guided deep-learning framework for pixel-level image fusion. *Information Fusion*, 91:205–214, 2023.

- [19] J. Liu, X. Fan, Z. Huang, G. Wu, R. Liu, W. Zhong, and Z. Luo. Target-aware dual adversarial learning and a multi-scenario multi-modality benchmark to fuse infrared and visible for object detection. In *Proceedings of the IEEE/CVF Conference on Computer Vision and Pattern Recognition*, pages 5802–5811, 2022.
- [20] Y. Liu, Y. Tian, Y. Zhao, H. Yu, L. Xie, Y. Wang, Q. Ye, and Y. Liu. Vmamba: Visual state space model. In *International Conference on Machine Learning*, 2024.
- [21] C. Lu, Y. Schroecker, A. Gu, E. Parisotto, J. Foerster, S. Singh, and F. Behbahani. Structured state space models for in-context reinforcement learning. *Advances in Neural Information Processing Systems*, 36, 2024.
- [22] J. Ma, W. Yu, P. Liang, C. Li, and J. Jiang. Fusiongan: A generative adversarial network for infrared and visible image fusion. *Information fusion*, 48:11–26, 2019.
- [23] J. Ma, H. Zhang, Z. Shao, P. Liang, and H. Xu. Ganmcc: A generative adversarial network with multiclassification constraints for infrared and visible image fusion. *IEEE Transactions on Instrumentation and Measurement*, 70:1–14, 2020.
- [24] E. Nguyen, K. Goel, A. Gu, G. Downs, P. Shah, T. Dao, S. Baccus, and C. Ré. S4nd: Modeling images and videos as multidimensional signals with state spaces. *Advances in neural information processing systems*, 35:2846–2861, 2022.
- [25] J. Peng, H. Zhao, Z. Hu, Y. Zhuang, and B. Wang. Siamese infrared and visible light fusion network for rgb-t tracking. *International Journal of Machine Learning and Cybernetics*, 14(9):3281–3293, 2023.
- [26] S. Peng, X. Zhu, H. Deng, Z. Lei, and L.-J. Deng. Fusionmamba: Efficient image fusion with state space model. *arXiv preprint arXiv:2404.07932*, 2024.
- [27] G. Piella and H. Heijmans. A new quality metric for image fusion. In *Proceedings 2003 international conference on image processing (Cat. No. 03CH37429)*, volume 3, pages III–173. IEEE, 2003.
- [28] G. Qu, D. Zhang, and P. Yan. Information measure for performance of image fusion. *Electronics letters*, 38(7):1, 2002.
- [29] A. Radford, J. W. Kim, C. Hallacy, A. Ramesh, G. Goh, S. Agarwal, G. Sastry, A. Askell, P. Mishkin, J. Clark, et al. Learning transferable visual models from natural language supervision. In *International conference on machine learning*, pages 8748–8763. PMLR, 2021.
- [30] J. Ruan and S. Xiang. Vm-unet: Vision mamba unet for medical image segmentation. *arXiv preprint arXiv:2402.02491*, 2024.
- [31] H. R. Sheikh and A. C. Bovik. Image information and visual quality. *IEEE Transactions on image processing*, 15(2):430–444, 2006.
- [32] H. Sun, Q. Liu, J. Wang, J. Ren, Y. Wu, H. Zhao, and H. Li. Fusion of infrared and visible images for remote detection of low-altitude slow-speed small targets. *IEEE Journal of Selected Topics in Applied Earth Observations and Remote Sensing*, 14:2971–2983, 2021.
- [33] L. Tang, J. Yuan, and J. Ma. Image fusion in the loop of high-level vision tasks: A semantic-aware real-time infrared and visible image fusion network. *Information Fusion*, 82:28–42, 2022.
- [34] L. Tang, J. Yuan, H. Zhang, X. Jiang, and J. Ma. Piafusion: A progressive infrared and visible image fusion network based on illumination aware. *Information Fusion*, 83:79–92, 2022.
- [35] L. Tang, H. Zhang, H. Xu, and J. Ma. Rethinking the necessity of image fusion in high-level vision tasks: A practical infrared and visible image fusion network based on progressive semantic injection and scene fidelity. *Information Fusion*, 99:101870, 2023.
- [36] W. Tang, F. He, Y. Liu, Y. Duan, and T. Si. Datfuse: Infrared and visible image fusion via dual attention transformer. *IEEE Transactions on Circuits and Systems for Video Technology*, 33(7):3159–3172, 2023.

- [37] A. G. Tri Dao. Transformers are ssms: Generalized models and efficient algorithms with structured state space duality. In *International Conference on Machine Learning*, 2024.
- [38] D. Wang, J. Liu, R. Liu, and X. Fan. An interactively reinforced paradigm for joint infrared-visible image fusion and saliency object detection. *Information Fusion*, 98:101828, 2023.
- [39] Z. Wang and A. C. Bovik. A universal image quality index. *IEEE signal processing letters*, 9(3):81–84, 2002.
- [40] H. Xie, Y. Zhang, J. Qiu, X. Zhai, X. Liu, Y. Yang, S. Zhao, Y. Luo, and J. Zhong. Semantics lead all: Towards unified image registration and fusion from a semantic perspective. *Information Fusion*, page 101835, 2023.
- [41] H. Xu, J. Ma, J. Jiang, X. Guo, and H. Ling. U2fusion: A unified unsupervised image fusion network. *IEEE Transactions on Pattern Analysis and Machine Intelligence*, 2020.
- [42] H. Xu, J. Ma, Z. Le, J. Jiang, and X. Guo. Fusiondn: A unified densely connected network for image fusion. In *Proceedings of the Thirty-Fourth AAAI Conference on Artificial Intelligence (AAAI)*, pages 12484–12491, 2020.
- [43] H. Zhang, H. Xu, X. Tian, J. Jiang, and J. Ma. Image fusion meets deep learning: A survey and perspective. *Information Fusion*, 76:323–336, 2021.
- [44] H. Zhang, H. Xu, Y. Xiao, X. Guo, and J. Ma. Rethinking the image fusion: A fast unified image fusion network based on proportional maintenance of gradient and intensity. In *Proceedings of the AAAI conference on artificial intelligence*, volume 34, pages 12797–12804, 2020.
- [45] J. Zhang, H. Liu, K. Yang, X. Hu, R. Liu, and R. Stiefelhagen. Cmx: Cross-modal fusion for rgb-x semantic segmentation with transformers. *IEEE Transactions on Intelligent Transportation Systems*, 2023.
- [46] X. Zhang and Y. Demiris. Visible and infrared image fusion using deep learning. *IEEE Transactions on Pattern Analysis and Machine Intelligence*, 2023.
- [47] W. Zhao, S. Xie, F. Zhao, Y. He, and H. Lu. Metafusion: Infrared and visible image fusion via meta-feature embedding from object detection. In *Proceedings of the IEEE/CVF Conference on Computer Vision and Pattern Recognition*, pages 13955–13965, 2023.
- [48] Z. Zhao, H. Bai, J. Zhang, Y. Zhang, S. Xu, Z. Lin, R. Timofte, and L. Van Gool. Cddfuse: Correlation-driven dual-branch feature decomposition for multi-modality image fusion. In *Proceedings of the IEEE/CVF conference on computer vision and pattern recognition*, pages 5906–5916, 2023.
- [49] Z. Zhao, H. Bai, J. Zhang, Y. Zhang, K. Zhang, S. Xu, D. Chen, R. Timofte, and L. Van Gool. Equivariant multi-modality image fusion. *CVPR*, 2024.
- [50] Z. Zhao, H. Bai, Y. Zhu, J. Zhang, S. Xu, Y. Zhang, K. Zhang, D. Meng, R. Timofte, and L. Van Gool. Ddfm: denoising diffusion model for multi-modality image fusion. In *Proceedings of the IEEE/CVF International Conference on Computer Vision*, pages 8082–8093, 2023.
- [51] Z. Zhao, S. Xu, C. Zhang, J. Liu, and J. Zhang. Bayesian fusion for infrared and visible images. *Signal Processing*, 177:107734, 2020.
- [52] Z. Zhao, S. Xu, C. Zhang, J. Liu, J. Zhang, and P. Li. Didfuse: Deep image decomposition for infrared and visible image fusion. In *IJCAI*, pages 970–976. ijcai.org, 2020.

A Appendix / supplemental material

A.1 Detailed Setup

Our model has three layers with channel numbers of [48, 96, 192], patch size of 4×4, and adjacent patches overlapping by one pixel. All experiments were conducted on an RTX 3090 Ti using AdamW as the optimizer and WarmupCosine for learning rate scheduling, with an initial learning rate of 0.0003, peaking at 0.0015, and decaying to 0.0006. The batch size was set to 20, and training was performed for 800 epochs. Input images were randomly cropped to 229×229 and augmented with random flipping.

RoadScene and M3FD datasets were randomly split, with 70% for training and the remainder for validation and testing, detailed in the code. For multi-modality object detection, we used Yolov5 with a pre-trained YOLOv5s model. The fusion results on M3FD were split 7:1:2 for training, validation, and testing, respectively. All methods were evaluated under identical experimental conditions, including the same random seeds, learning rates, and dataset splits. Each method was trained for 40 epochs on its fusion images using Yolov5, with the best model selected based on validation performance and evaluated on the test set.

For ablation studies, we replaced the fusion module and adjusted its layer count and channel numbers to match the parameter count of our method. For the ADD replacement method, we adjusted the encoder and decoder channel numbers to modulate model size. All ablation experiments were conducted under the same experimental conditions to ensure fairness.

A.2 More Qualitative Comparison

In Fig.6,7,8,9,10,11, we provide additional qualitative comparisons to demonstrate the effectiveness of our method. Our approach does not rely on favoring a specific modality for fusion but adaptively integrates information. For instance, in Fig.8, the visible light image shows a blurry person, while the infrared image highlights the person clearly. Our method adaptively perceives this, unlike other methods, except DeFusion, which fail to highlight the salient target effectively. However, DeFusion performs poorly on edge details, introducing artifacts not present in the original image, such as the utility pole in the red box. In Fig.6, the person in the visible image stands out against the background, whereas the infrared image is blurrier. Other methods favor the infrared, retaining its information and causing the originally clear person to become blurred. Our method preserves infrared details on the face and visible information for the rest, making the person more prominent than in the visible image. Additionally, our method retains more complete details, aligning better with human perception. These examples demonstrate that our method does not favor one modality over another but truly achieves adaptive integration to highlight salient information.

A.3 Cross SS2D

In this section, we further explain the parameters of Cross SS2D in detail. First, we elaborate on the operation of Inter in Cross SS2D. Taking $\text{Inter}(S_{BI}, S_{BV})(\mathbf{x})$ as an example, we assume the input sequence is $\mathbf{x} = [I_1, V_1, I_2, V_2, \dots, I_L, V_L]$, where V_i and I_i represent the i -th patches of the visible and infrared modalities, respectively, for $i \in \{1, 2, \dots, L\}$. The Inter operation arranges the parameters into a sequence of length $2L$: $\text{Inter}(S_{BI}, S_{BV}) = [S_{BI}, S_{BV}, S_{BI}, S_{BV}, \dots, S_{BI}, S_{BV}]$, where the S_{BI} and S_{BV} are linear layers. For the linear layers, the Inter operation simply aligns the same modality’s linear layer with the sequence positions. Finally, $\text{Inter}(S_{BI}, S_{BV})(\mathbf{x}) = [S_{BI}(I_1), S_{BV}(V_1), S_{BI}(I_2), S_{BV}(V_2), \dots, S_{BI}(I_L), S_{BV}(V_L)]$, meaning that the corresponding patches are input into their respective linear layers to compute the corresponding B parameters.

We denote B as $B = [B_{I1}, B_{V1}, B_{I2}, B_{V2}, \dots, B_{IL}, B_{VL}]$, where B_{Ii} and B_{Vi} represent the B parameters for the i -th patches in the sequence, with $i \in \{1, 2, \dots, N\}$. Where, subscripts V and I denote the visible and infrared modalities, respectively. It’s worth noting that the Inter parameter merely arranges the linear layers without duplicating parameters, indicating the presence of only two sets of linear layer parameters.

Table 5: Comparison of the average Δ for the two modalities across different layers.

	$\bar{\Delta}_I$	$\bar{\Delta}_V$
Layer1	0.0014	-0.0056
Layer2	-3.999	-5.885
Layer3	-6.308	-19.811

A.3.1 Interpretation of \mathbf{A}

According to the theory of parameter \mathbf{A} in Mamba[6], parameter \mathbf{A} can also become selective. However, following Mamba’s design philosophy, we make parameter \mathbf{A} independent of the input and shared between the two modalities. Based on the discretization formula $\bar{\mathbf{A}} = \exp(\Delta\mathbf{A})$, making Δ selective is sufficient for $\bar{\mathbf{A}}$ to be selective, thus making \mathbf{A} selective is unnecessary. Similarly, for two different modalities, it is not required to set separate parameter \mathbf{A} for each; the respective parameters Δ are sufficient to distinguish their respective $\bar{\mathbf{A}}$ for different modalities.

A.3.2 Interpretation of Δ

Similar to parameter \mathbf{B} , Δ can be expressed as $\Delta = [\Delta_{I1}, \Delta_{V1}, \Delta_{I2}, \Delta_{V2}, \dots, \Delta_{IL}, \Delta_{VL}]$. Generally, Δ controls the relationship between the current and previous inputs. In SSM, Δ represents the interval after discretizing a continuous signal. Larger values of Δ indicate a greater emphasis on the current input, while smaller values indicate the opposite. Notably, the infrared parameter Δ_I controls the interval for different spatial positions of different modalities, whereas Δ_V controls the interval for the same spatial position of different modalities.

For the l -th layer of CMSA, we denote $\bar{\Delta}_I^{(l)}$ and $\bar{\Delta}_V^{(l)}$, $l \in \{1, 2, 3\}$ as the average sizes of the Δ parameters for infrared and visible in l -th layer. As shown in Table.5, we conducted experiments on the MSRS test set, calculating the average Δ parameter values for infrared and visible across all CMSABs in each layer to obtain $\bar{\Delta}_I^{(l)}$ and $\bar{\Delta}_V^{(l)}$, $l \in \{1, 2, 3\}$. Due to the frequent inter-modal and spatial interactions in Cross SS2D, this interleaving Δ effectively controls the transmission of information between modalities and spatial locations.

Most of the time, $\bar{\Delta}_I^{(l)}$, where $l \in \{1, 2, 3\}$, represents the interval between adjacent patches of different modalities in space. As shown in Table.5, in all layers, $\bar{\Delta}_I^{(l)}$ is greater than $\bar{\Delta}_V^{(l)}$. Larger values indicate greater differences between inputs over time, emphasizing current position information and compressing past information to capture spatial information. This is because the information difference between spatially adjacent patches is greater than the patches of different modalities in the same position. For example, infrared and visible images at the same spatial position may capture the same object, exhibiting strong complementarity.

Conversely, $\bar{\Delta}_V^{(l)}$, where $l \in \{1, 2, 3\}$, represents the interval between patches of the same position but different modalities. These values are significantly smaller than $\bar{\Delta}_I^{(l)}$, indicating that the model prefers previous information and selects a smaller portion of complementary information from the current position. SSM reconstructs signals better when they are closer, suggesting that $\bar{\Delta}_V^{(l)}$ controls the acquisition of complementary information between patches of different modalities at the same position.

We also observe that the value of both $\bar{\Delta}_I$ and $\bar{\Delta}_V$ decreases with increasing layers. This indicates that as the semantic level increases, the model tends to consider each patch’s information more deeply, forgetting the current hidden state less and remembering past information more.

A.3.3 Interpretation of \mathbf{B} and \mathbf{C}

\mathbf{B} and \mathbf{C} regulate the input-to-hidden state and hidden state-to-output information flow, respectively. We employ distinct parameters for each modality to compute \mathbf{B} and \mathbf{C} . This facilitates the precise extraction and retention of complementary modality and spatial information from the hidden state, tailored to the specific characteristics of each modality’s information.

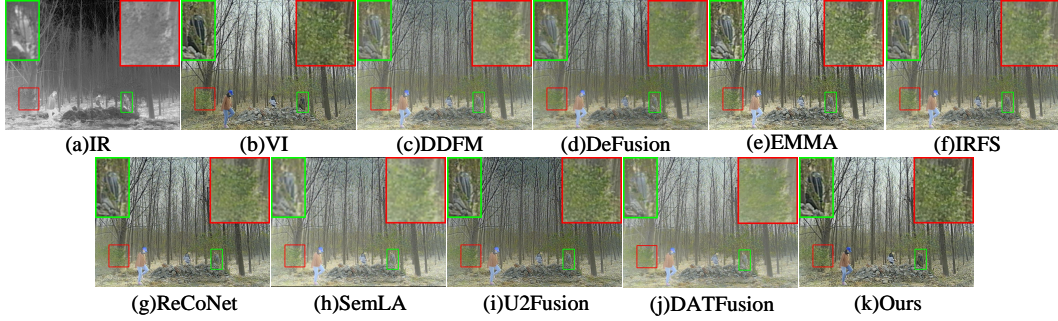


Figure 6: Qualitative comparison of the original images and the results of all methods on "01416" from M3FD[19].

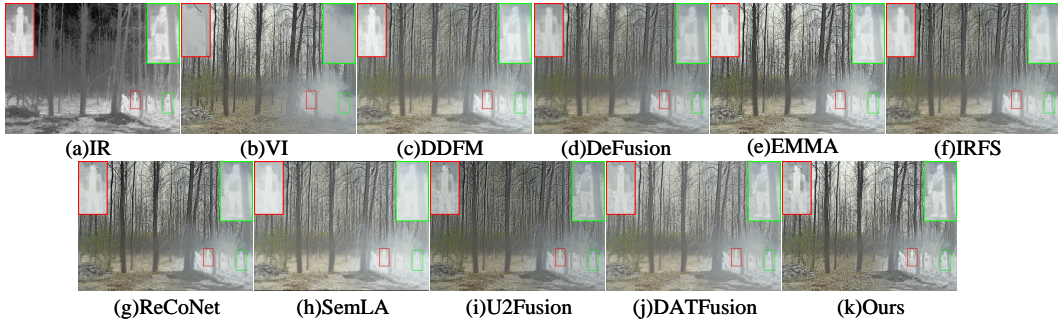


Figure 7: Qualitative comparison of the original images and the results of all methods on "01432" from M3FD[19].

B Limitation

Thanks to the pre-trained ResNet50 model, we can dynamically integrate useful information from two original images. However, relying solely on a single ResNet50 network to mimic human vision introduces inherent biases from the pre-trained model. Additionally, as most classification networks are trained on datasets with fixed categories (e.g., ImageNet-1K), their decision layers are limited by these categories. Yet, real-world salient objects exhibit diversity beyond these limitations. Using multiple pre-trained networks for integration as a form of supervision and employing networks with "almost infinite categorization capabilities" like CLIP[29] as supervision signals will be left for future exploration. Nonetheless, we provide a new loss function design idea and a new single-stage fusion module, which may offer more insights for the image fusion community.

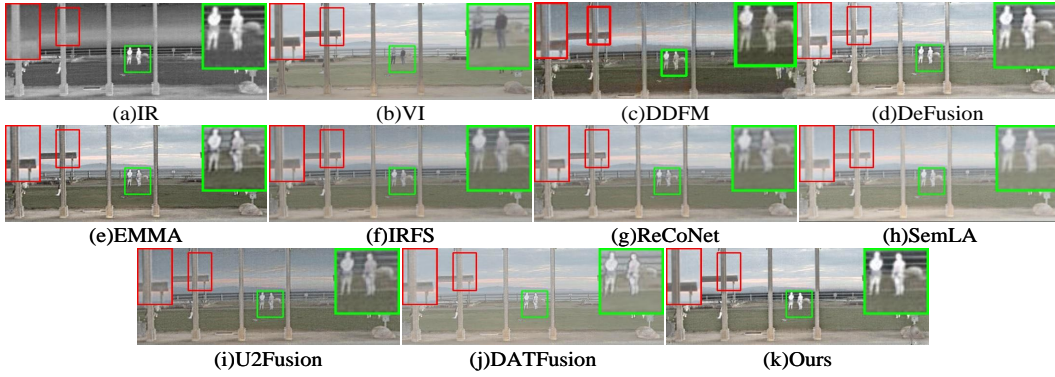


Figure 8: Qualitative comparison of the original images and the results of all methods on "FLIR_06621" from RoadScene[42].

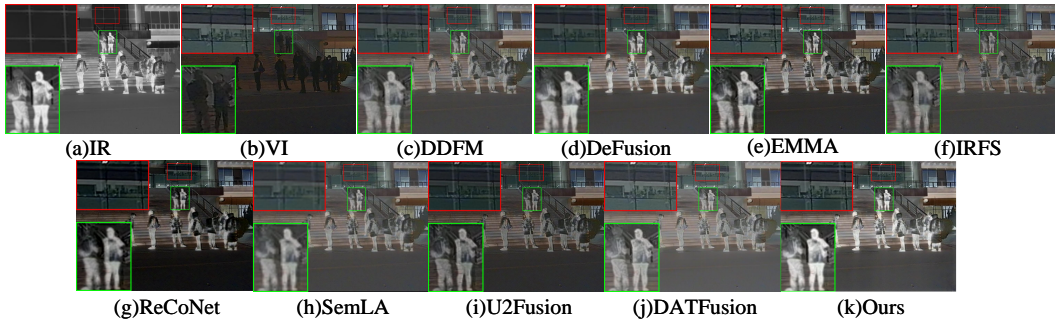


Figure 9: Qualitative comparison of the original images and the results of all methods on "02119" from M3FD[19].

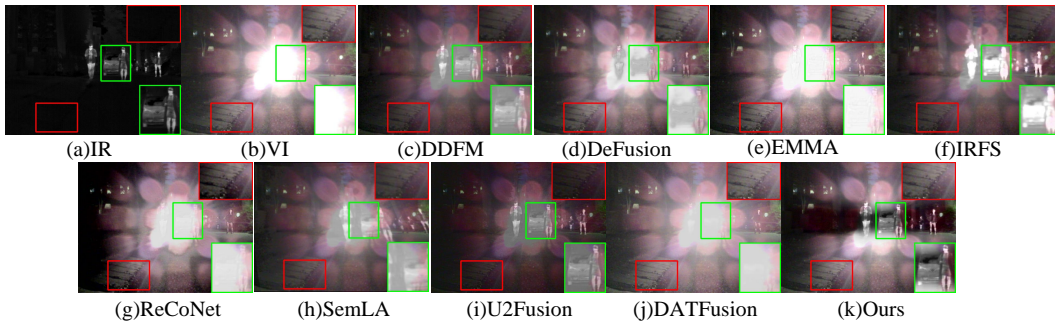


Figure 10: Qualitative comparison of the original images and the results of all methods on "00037N" from MSRS[34].

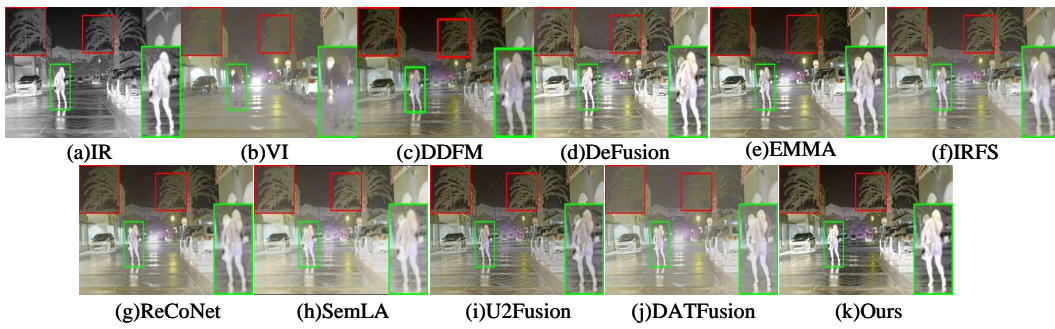


Figure 11: Qualitative comparison of the original images and the results of all methods on "FLIR_08954" from RoadScene[42].